

## CONVECTIVE INSTABILITIES OF ELECTROKINETIC FLOWS IN A CROSS-SHAPED MICROCHANNEL

Jonathan D. Posner and Juan G. Santiago

Department of Mechanical Engineering, Stanford University, Stanford, CA 94305

JONATHAN.POSNER@STANFORD.EDU

### ABSTRACT

Electrokinetic instabilities (EKI) in cross-shaped channels are relevant to injections for field amplified sample stacking, flow intersections in multi-dimensional assay devices, and electrokinetic systems with indeterminate sample chemistry. Electrokinetic instabilities are generated by a coupling of electric fields and ionic conductivity gradients. This coupling results in an electric body force in the bulk liquid that can generate temporal, convective, and absolute flow instabilities. In this work, we perform a parametric experimental study of convective instabilities in cross-shaped microchannels using epifluorescence microscopy and digital imaging. We report coherent flow structures and show that the critical electric field for instability is both a function of center-to-sheath conductivity ratio and applied field ratio. Finally, we quantify the degree of mixing rate of electrokinetically unstable flows with time-average probability density functions of concentration profiles.

### INTRODUCTION

Electrokinetic instabilities (EKI) are generated by a coupling of electric fields and ionic conductivity gradients. The coupling of an electric field and a conductivity gradient results in an electric body force (per unit volume) of the form  $(\varepsilon \bar{E} \cdot \nabla \sigma) \bar{E}$ , where  $\varepsilon$ ,  $\bar{E}$ , and  $\sigma$  are the local permittivity, electric field, and ionic conductivity, respectively. These conditions are relevant to on-chip electrokinetic flows with conductivity gradients, such as sample injection for field amplified sample stacking [1], low-Reynolds number micromixing [2], multidimensional assays, and electrokinetic systems with indeterminate sample chemistry. Electrokinetic flows become unstable when the ratio of the electric body force to the viscous force in the flow exceeds a critical value [3]. We have presented parametric experimental studies and detailed models for EKI in systems with temporal instabilities in long-thin capillaries [3] and convective instabilities in high-aspect-ratio T-junction microchannels [4]. These studies provide a fundamental understanding of EKI's, identify key controlling parameters, and present predictive simulations. In the current work, we

present a parametric experimental study of a convective EKI in a cross-shaped microchannel.

### EXPERIMENTAL METHODOLOGY

We obtained instantaneous concentration fields of rhodamine B and 70 kDa dextran-conjugated rhodamine B using epifluorescence microscopy and CCD camera (Roper Scientific, Trenton, NJ) imaging. Figure 1 shows the experimental setup. Experiments were performed in isotropically etched glass channels 50  $\mu\text{m}$  wide and 20  $\mu\text{m}$  deep (Micalyne Inc, Alberta, Canada). Electrical potentials were applied to channel reservoirs and synchronized to the CCD image acquisitions using a high voltage sequencer (LabSmith, Livermore, CA). The exposure time of each image is controlled by a liquid crystal, video-rate shutter (Displaytech, Longmont, CO). A 20x, NA = 0.45 ELWD objective (Nikon, Japan), epifluorescence filter cube (excitation at 540 nm, emission at 625 nm-Chroma, Rockingham, VT), and mercury bulb are used to image fluorescence onto the plane of the CCD sensor.

An instantaneous image of the stable base state flow is shown in Figure 2(a). The high conductivity solution is in the center, dyed stream. We define the electric field in each channel as the potential applied between end-channel reservoirs divided by the appropriate channel lengths. The south-channel field,  $E_s$ , is the potential difference between the south (bottom of image) well and the east (left side of image), grounded well divided by a total 9 mm channel length. The west-channel field,  $E_w$ , is the applied field associated with the potential difference between the west well and the east well (an 8 mm distance). We define  $\beta$  as the ratio of the west and south applied fields,  $E_w/E_s$ .

The stock aqueous buffered solutions consisted of filtered deionized water (Fisher Scientific W2-20, Fairlawn, NJ) and 10 mM of HEPES hemisodium salt (Sigma Aldrich). The pH of the buffered solutions were 7.5 as measured using a pH meter (Corning, Corning, NY). Potassium chloride (Sigma Aldrich, St. Louis, MO) was added to the stock solutions to obtain desired conductivities. The conductivity of the west well solution,  $\sigma_w$ , remained constant throughout the experiments and

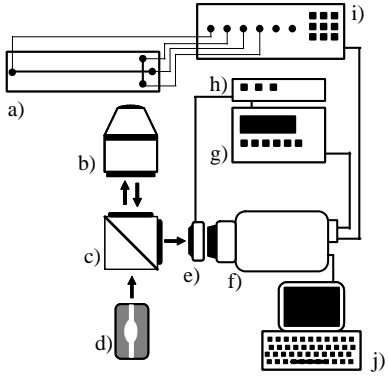


Figure 1. Experimental setup showing a) glass microchip; b) objective; c) filter cube; d) mercury bulb illumination source; e) liquid crystal shutter; f) charged couple device camera; g) digital delay; h) liquid crystal driver; i) high voltage sequencer; and j) computer.

was measured as 40 mS/cm using a conductivity meter (CON Oakton Instruments, Vernon, IL). The north and south well solution conductivities,  $\sigma_s$ , were identical and were varied from 0.4 mS/cm to 40 mS/cm. We define the conductivity ratio,  $\gamma$ , as  $\sigma_w / \sigma_s$ , which varied from 1-100. To visualize fluid motion, 10 mM of electrically neutral, rhodamine B dye was added to the west well solution. To improve the clarity of the visualizations shown in Figure 2 (and for this experimental alone), high molecular weight (70 kDa), dextran conjugated rhodamine B dye was used at a concentration of 10mM.

We recorded data for nine values of  $\gamma$  varying from 1-100, eleven values of  $\beta$  varying from 0.85-1.6, and applied fields spanning values that corresponded to stable and highly unstable flow (typically  $E_s = 275$  V/cm to 600 V/cm). For a given experiment (corresponding to fixed  $\gamma$  and  $\beta$ ) we slowly varied the applied field  $E_s$  from an initial, low field to a field 333 V/cm greater than the initial field in 100 equal increments. The initial field for each experiment varied as the critical field for instability strongly depends on  $\gamma$ . For each field, 200 images were recorded with an exposure time of 1 msec at a rate of 115 frames per second. Images of scalar concentration are corrected for background and flat-field non-uniformities with the equation,

$$\hat{I} = \frac{I(x, y) - I(x, y)_{back}}{I(x, y)_{flat} - I(x, y)_{back}} \quad (1)$$

where the subscripts *flat* and *back* denote the flat-field image and background images, respectively. The elapsed time for each experiment was 4 minutes.

## RESULTS AND DISCUSSION

We first present a brief characterization of the base state flow. For stable flow regimes, the width of the center stream is a function of both  $\gamma$  and  $\beta$  as well as electrolyte chemistry as the electroosmotic mobilities of the channels are a function of conductivity and pH. Figure 2(a) shows the base state scalar field for  $\gamma = 10$ ,  $\beta = 1.2$ , and  $E_s = 0.3$  kV/cm. In all the

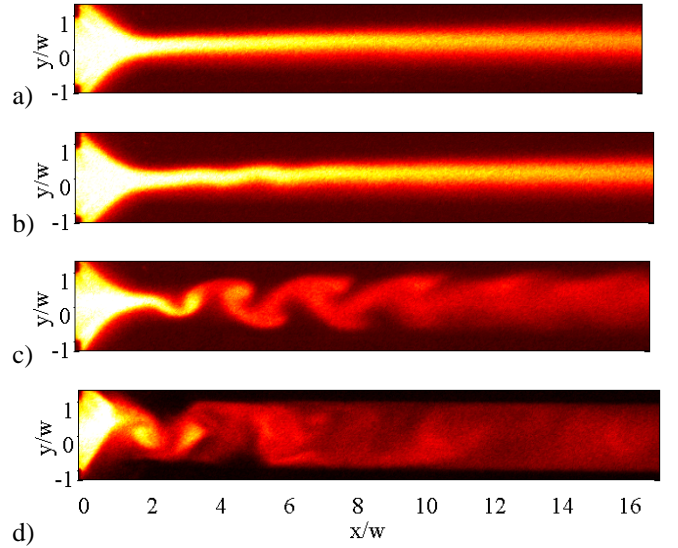


Figure 2. Epifluorescence images of 70 kDa dextran-conjugated rhodamine B tracer electrokinetically injected in a cross-shaped microchannel. The dyed stream enters the cross from the left hand edge, flows right (in direction of applied electric field), and is “pinched” into the long channel region by flows from vertical channels centered at  $x/w = 1$ . The channel half-height,  $w$ , is 25  $\mu\text{m}$ . The dyed stream conductivity is 10 times that of the sheathing flow streams: a) Flow is stable for  $E_s = 0.30$  kV/cm; b) at 0.35 kV/cm small disturbances are detected but do not grow as they convect downstream; c) at  $E_s = 0.47$  kV/cm, flow demonstrates strong convective instability and flow field is periodic and deterministic; and d) at  $E_s = 0.70$  kV/cm, flow demonstrates absolute instability where disturbances propagate upstream.

experiments, we applied potentials in the north and south wells so that the fields in the north and south channels were equal and the flow was symmetric about the  $x$ -axis. We define the measured spanwise ( $y$ -direction) width of the focused stream as the full width at  $1/e^2$  of the max intensity at a downstream location of  $x/w = 2$ . For  $\gamma = 100$ ,  $\text{pH} = 7.5$ , and  $E_s = 0.275$  kV/cm the least-squares linear fit of the center stream width normalized by the channel half-height is,

$$h/w = 1.14\beta - 0.12 \quad (2)$$

where  $w$  is the channel half-height. The linear fit results in a *r-squared* value equal to 0.937. The center stream width is also a function of  $\gamma$  and pH, but in this work we only report data as a function of  $\beta$  for a single  $\gamma = 100$  and a pH of 7.5.

Next, we describe qualitative features of the onset of the instability. Images of corrected scalar concentration recorded at four applied fields are shown in Figure 2. Figure 2(a) shows the base state flow (stable case). When the applied electric field exceeds a critical value, a sinuous pattern in the dye concentration develops and advects downstream. For electrical fields slightly below the critical field,  $E_s = 0.35$  V/cm, the amplitude of disturbances diminish in size and strength as they convect downstream as show in Figure 2(b). At fields in excess

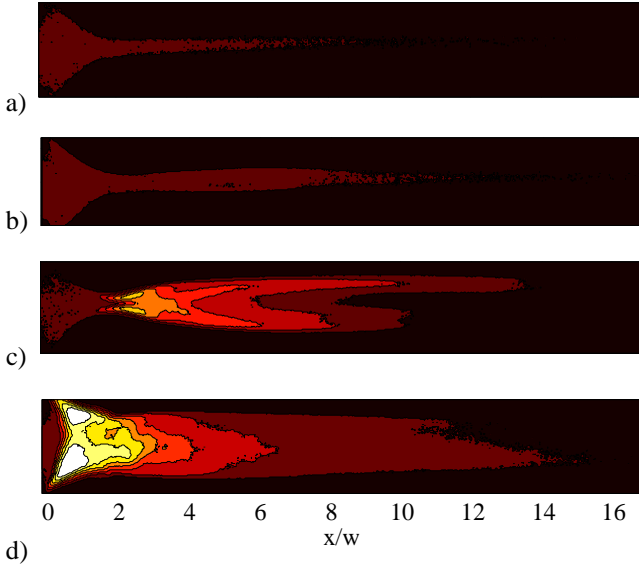


Figure 3. Root mean square of tracer concentration. a) Flow is stable for  $E_s = 0.30$  kV/cm; b) at  $E_s = 0.35$  kV/cm small disturbances are detected but do not grow as they convect downstream; c) at  $E_s = 0.47$  kV/cm, there is a strong convective instability and flow field is periodic and deterministic; and d) at  $E_s = 0.70$  kV/cm, disturbances propagate upstream.

of the critical field,  $E_s = 0.47$  V/cm, the disturbance grows along the downstream direction forming coherent flow structures as shown in Figure 2(c). Figure 2(d) shows a strong instability at  $E_s = 0.70$ , where the flow patterns appear to be chaotic and disturbances move upstream to the intersection region of the channel.

Figure 3 shows root mean square (RMS) scalar fields computed over 200 images for the scalar fields shown in Figure 2. For each applied field, the RMS is defined as,

$$RMS(x, y; E_s) = \sqrt{\frac{\sum_{i=1}^n (\hat{I}_i(x, y; E_s) - \overline{\hat{I}_i(x, y; E_s)})^2}{n-1}} \quad (3)$$

where  $n$  is the number of images and the over bar denotes an ensemble average over  $n$  images. Figure 3(a) shows the RMS field of the base state for  $\gamma = 10$ ,  $\beta = 1.2$ , and  $E_s = 0.3$  kV/cm. At  $E_s = 0.35$  kV/cm we see the influence of small disturbances on the RMS field (Figure 3b). At  $E_s = 0.47$  kV/cm, the spanwise growth of the RMS envelope is approximately exponential and then bound by the channel walls as shown in Figure 3(c). A region of exponential growth is consistent with linear stability theory where the amplitude of convective instabilities grows as  $e^{-K(x/w)}$ , where the nondimensional (channel half-height) growth rate is  $(-K)$ . We can define the region of high RMS as that bounded by an RMS contour equal to the area averaged RMS value. Using this definition, the nondimensional spatial growth rate,  $(-K)$ , of the convective instability in Figure 3(c) is 0.2. The image in Figure 3(d), obtained at  $E_s = 0.70$  kV/cm, shows strong scalar fluctuations in the upstream, intersection region of the channel.

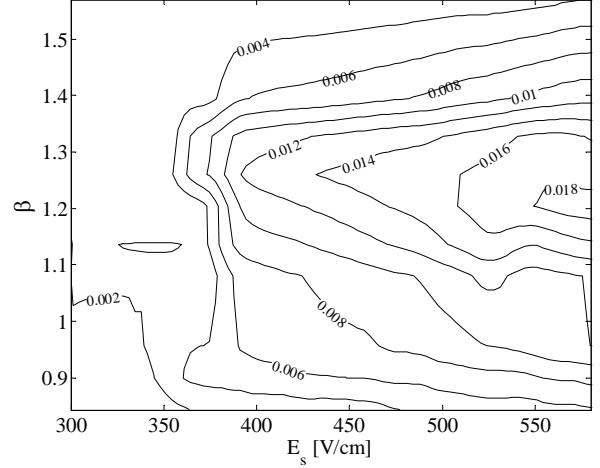


Figure 4. Contour map of area averaged scalar perturbation energy,  $\langle En_s \rangle$  for  $\gamma = 100$  as a function of applied field  $E_s$  and west-to-south electric field ratio,  $\beta$ . The flow is most unstable for values of  $\beta$  near 1.2.

Next, we explore the effect of the center stream width on the stability of the flow. Figure 4 is a contour map of the area average scalar perturbation energy,  $\langle En_s \rangle$ , as a function applied field  $E_s$  and field ratio,  $\beta$ . We adopt the definition of Chen et al. [1] for scalar perturbation energy,  $En_s$ , as the square of the RMS intensity. The contour map is rendered from 11 values of  $\beta$  and 100 discrete applied fields. Each RMS value on the map is determined from 200 instantaneous images and area averaged over a region of  $50 \times 512$  pixels. For each value of  $\beta$ , the area average scalar perturbation energy monotonically increases with increasing field. The instability is strongest for  $\beta$  values near 1.2 where the center stream width is nearly equal to the sheath stream widths (i.e., where the center stream takes up approximately one third of the channel). The strength of the instability decreases as the value of  $\beta$  deviates from 1.2 where either the center stream or sheath flows encompass the majority of the flow channel. We attribute this behavior to the strength of conductivity gradients for various  $\beta$ .  $\beta = 1.2$  is associated with flows with maximum conductivity gradients as discussed below.

We determined the value of the critical field required for an instability, for a given conductivity ratio  $\gamma$ , by slowly ramping the applied field  $E_s$  from an initial, low value and monitoring RMS fluctuations of intensity. Figure 5 shows the area average scalar perturbation energy,  $\langle En_s \rangle$ , as a function of applied field

for various center-to-sheath conductivity ratios,  $\gamma$ . For low fields, the area average perturbation energy is that of the base state and has a typical value of 0.001. As electric fields increase, perturbation energy undergoes a dramatic rise at the onset of instability to values well above 0.005. We define the critical electric field as the applied field that results in an area average scalar perturbation energy that is twice that of the (stable) state. A summary of these experiments is shown in

Figure 6 which shows the critical electric fields as a function of conductivity ratio.

We can estimate the scaling of critical field with  $\gamma$  by applying the scaling relations suggested by Chen et al [1]. Chen et al. proposed a scaling of the form

$$E_c = \left[ Ra_e \frac{\delta \mu D_{eff}}{w \epsilon d^2} \right]^{\frac{1}{2}} \frac{\gamma+1}{\gamma-1} \quad (4)$$

where  $Ra_e$  is the critical electric Rayleigh number,  $\delta$  is the diffusive length scale,  $w$  is the channel half width,  $\mu$  is the fluid viscosity,  $D_{eff}$  is the effective diffusivity, and  $d$  is the depth of the channel. The Rayleigh number is a ratio of electric body forces to viscous forces in the flow. Although Chen's analysis was for flow in a T-shaped microchannel with a single interface, this type of scaling suggests that critical field should scale as  $(\gamma+1)/(\gamma-1)$ . Figure 6 shows the  $(\gamma+1)/(\gamma-1)$  scaling in comparison with the experimental data.

The data presented in Figure 4 gives insight into the critical field as a function of  $\beta$ . The contour  $\langle En_s \rangle = 0.004$  in Figure 4 defines the critical field as a function of  $\beta$ . For  $\beta$  values between roughly 1.5 and 0.9, the  $\langle En_s \rangle = 0.004$  contour is nearly vertical and suggests that the critical field is a weak function of  $\beta$ . Outside of this range, the critical field increases rapidly and is a strong function of  $\beta$  (nearly horizontal regions of this contour). This dependence of critical field on  $\beta$  can be related to the characteristic diffusion thicknesses over which strong conductivity gradients occur. Consider a typical diffusive length scale,  $\delta$ , for this problem, based upon an advective electroosmotic velocity,

$$\delta = \sqrt{\frac{LD_{eff}}{u_{eo}}} \quad (5)$$

where  $u_{eo}$  is the electroosmotic velocity in the channel and  $L$  is a characteristic advective length scale. Using the effective diffusivity of KCl,  $D_{eff} = 2 \cdot 10^{-9} \text{ m}^2 \text{ s}^{-1}$ , the channel half width of  $25 \text{ } \mu\text{m}$ , and an electroosmotic velocity of  $2.1 \text{ mm/s}$  at  $E_s = 0.4 \text{ kV/cm}$ , the diffusive length scale at  $x/w = 2$  is  $6.9 \text{ } \mu\text{m}$ . We chose  $x/w = 2$  location as the characteristic length because it is the approximate location of maximum RMS intensity for critical field conditions. Given this definition of  $\delta$ , the equations,

$$\frac{w}{\delta} \left( 1 - \frac{h}{2w} \right), \frac{h}{2\delta} \approx 1 \quad (6)$$

describe the respective conditions under which the sheath flow and center stream widths are on the order of the diffusion thickness. The conditions of equations 5 are satisfied for  $\beta = 1.4, 0.6$  which roughly correspond with the regions where stability becomes a strong function of  $\beta$  in Figure 4. This analysis suggests that the largest conductivity gradients are limited by the smallest diffusive length scale allowed by the value of  $\beta$ . The smallest diffusive length scale is determined by center stream width for thin center streams (small  $\beta$ ) and by sheath stream thickness for thick center streams (large  $\beta$ ).

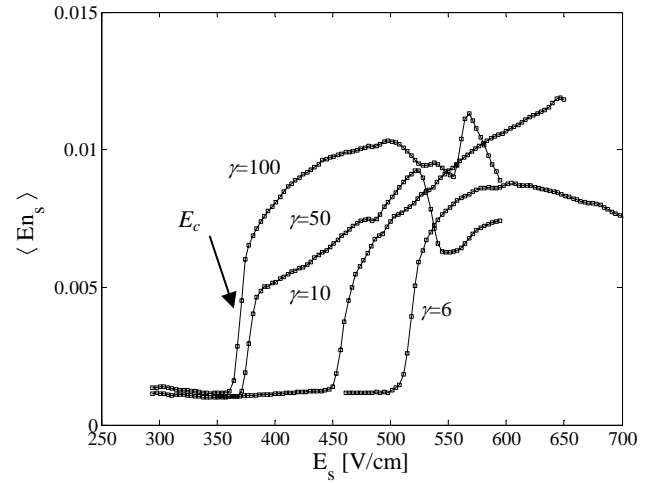


Figure 5. Area averaged scalar perturbation energy,  $\langle En_s \rangle$  as a function of applied electric field shown for center-to-sheath conductivity ratios  $\gamma = 100, 50, 10, 6$ ; and a west-to-south field ratio  $\beta = 1.125$ . The scalar perturbation energy dramatically increases at a critical field,  $E_c$ , specific to each  $\gamma$

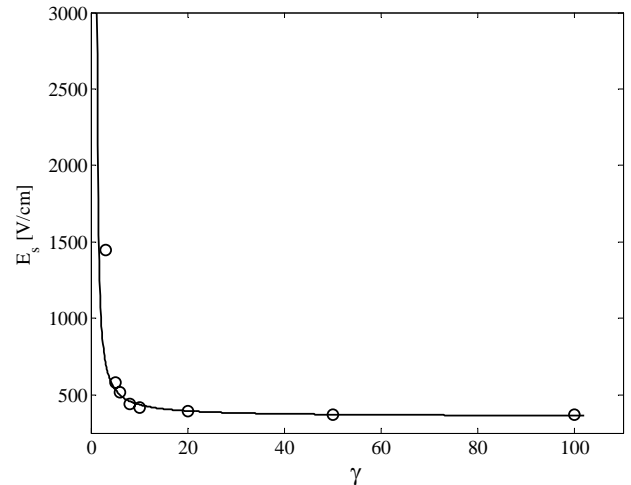


Figure 6. Critical electric field (required for instability) plotted as a function of center-to-sheath stream conductivity ratio,  $\gamma$ .

It is evident from the RMS intensity fields of Figure 3 that the origin of disturbances in the field moves upstream as the applied field increases. Figure 7 shows the location of the maximum RMS intensity as a function of applied field for various values of the west-to-south electric field ratio,  $\beta$ . The max RMS location asymptotes to large downstream locations for conditions below the critical electric field. For near-critical fields, the maximum RMS intensity is in the range of  $x/w = 2$  to 3. For fields greater than the critical value, the position of max RMS decreases approximately linearly with increasing field strength. The location of max RMS gives some insight to an experimental identification of the demarcation between convective and absolute instability. Physically, an absolute

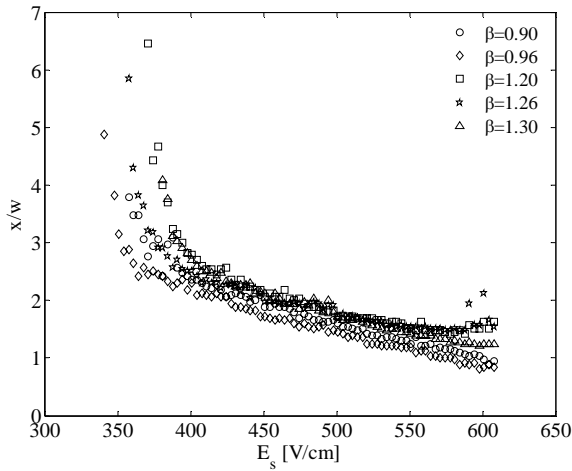


Figure 7. Position,  $x/w$ , of maximum perturbation energy location as function of applied field  $E_s$  for several values of west-to-south field ratio  $\beta$ .

instability is characterized by disturbances with a group velocity that exceeds the flow's advective velocity. In EKI, this occurs at the point where the electroviscous velocity produced by electric body forces in the flow exceeds the magnitude of advective velocity provided by electroosmosis. This results in a condition where disturbances can travel upstream [4].

Lastly, we quantify the degree of electrokinetic instability mixing using time-averaged probability density functions of concentration profiles [2]. Probability density functions (PDF's) of normalized scalar image intensity are shown in Figure 3 for eight axial locations and three applied fields. Highly bimodal distributions indicate unmixed conditions (e.g., the  $x/w=3$  distribution in top of Figure 3). Single mode distributions with high probability densities near mid-level intensity values (e.g.,  $x/w=15$  distribution at the bottom of Figure 3) indicate well-mixed regions. These results suggest that strong electrokinetic instabilities mix rapidly and over short distances.

## CONCLUSION

We have performed a parametric experimental study of convective instabilities in cross-shaped microchannels using epifluorescence microscopy and digital imaging. We report coherent flow structures and show that the critical electric field for instability is both a function of center-to-sheath conductivity ratio and applied field ratio. The origin of the instability moves upstream with increasing applied field. Tracking of the instability origin may be useful in detecting the transition between convective absolute instability in this flow. Finally, we quantified the degree of electrokinetic instability mixing using time-averaged probability density functions of concentration profiles. Highly unstable conditions lead to rapid mixing over short distances.

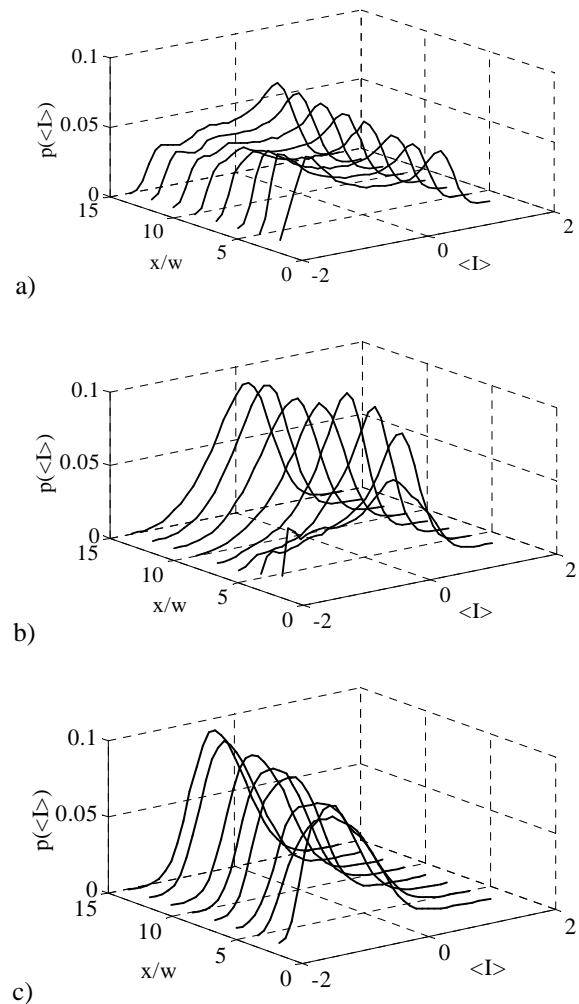


Figure 8. Probability density functions,  $p(\langle I \rangle)$ , of normalized image intensity,  $\langle I \rangle$ , at eight axial locations and for the three applied fields,  $E_s = 0.30, 0.47,$  and  $0.7$  kV/cm. The distributions were generated from 200 images.

## ACKNOWLEDGEMENTS

This work was supported by an NSF CAREER Award (J.G.S.) with Dr. Michael W. Plesniak as contract monitor. The authors thank Dr. Hao Lin and Michael Oddy for insightful discussions.

## REFERENCES

1. B. Jung, R. Bharadwaj, J.G. Santiago *Thousandfold signal increase using field-amplified sample stacking for on-chip electrophoresis*, Electrophoresis, 2004, 24.
2. M.H. Oddy, J.G. Santiago, J. C. Mikkelsen, *Electrokinetic Instability Micromixing*, Analytical Chemistry, 2001, 73.
3. H. Lin, B. D. Storey, M.H. Oddy, C.H. Chen, J.G. Santiago, *Instability of electrokinetic microchannel flows with conductivity gradients*, Physics of Fluids, 2004, 16.

4. C.H. Chen, H. Lin, S.K. Lele, J.G. Santiago, *Convective and absolute electrokinetic instability with conductivity gradients*, J of Fluid Mechanics, In press, 2004.